Direct observation of spin diffusion enhanced nonadiabatic spin torque effects in rare-earth-doped permalloy

Pascal Krautscheid,[1,2] Robert M. Reeve,[1,2] Daniel Schönke,[1] Isabella Boventer,[1,3] Andrés Conca,[4] Andrii V. Chumak,[4] Burkard Hillebrands,[4] Jonathan Ehrler,[5] Julia Osten,[5] Jürgen Fassbender,[5,6] and Mathias Kläui[1,2,*]

[1]*Institut für Physik, Johannes Gutenberg-Universität Mainz, 55128 Mainz, Germany*
[2]*Graduate School of Excellence Materials Science in Mainz, 55128 Mainz, Germany*
[3]*Fakultät für Physik, Karlsruher Institut für Technologie, 76131 Karlsruhe, Germany*
[4]*Fachbereich Physik and Landesforschungszentrum OPTIMAS, Technische Universität Kaiserslautern, 67663 Kaiserslautern, Germany*
[5]*Helmholtz-Zentrum Dresden-Rossendorf, Institute of Ion Beam Physics and Materials Research, 01328 Dresden, Germany*
[6]*Institute for Physics of Solids, Technische Universität Dresden, 01069 Dresden, Germany*

The relation between the nonadiabaticity parameter β and the damping parameter α is investigated in permalloy-based microdisks. In order to determine β, high-resolution imaging of the current-induced vortex-core displacement is performed using scanning electron microscopy with polarization analysis. The materials properties of the films are varied via rare-earth Dy doping, leading to a greatly enhanced damping, while retaining the same spin configuration for the confined vortex state. A clear trend to much higher nonadiabaticity values is seen for the higher doping levels and an averaged value of $\beta = (0.29 \pm 0.15) \times 10^{-2}$ is determined for 1.73% Dy doping, compared to $(0.067 \pm 0.014) \times 10^{-2}$ which is extracted for pure permalloy. This is supportive of a similar scaling of β and α in this system, pointing to a common origin of the spin relaxation which is at the heart of nonadiabatic transport and the dissipation of angular momentum that provides damping, in line with theoretical calculations.

Today's prevalent data-storage devices rely on a controlled modification of the magnetization of thin ferromagnetic films on a nanometer scale. Conventionally, this is achieved via current-generated magnetic fields; however, manipulation of the magnetic state via the spin-torque effect yields favorable scaling in regard to the electrical-power consumption on size downscaling. Hence, the latter effect is now employed in state-of-the-art spin-transfer-torque magnetoresistive random access memory (STT-MRAM) which relies on spin-current-induced switching of mesoscopic magnetic elements [1] and which has been proposed to propagate magnetic domain walls (DWs) in racetrack-memory-type devices [2]. Another proposed architecture for a magnetic random-access-memory architecture is based on magnetic elements in the so-called vortex state, where the energetically degenerate states with different polarities and/or chiralities can be employed to encode data [3,4]. It has been demonstrated that current-induced spin torques can displace the vortex core of such an element or generate steady oscillations of the system [5,6] in addition to switching the state. To theoretically model the spin torques, the Landau-Lifshitz-Gilbert equation describing the time (t) evolution of the magnetization, $\vec{m}$, is extended to incorporate two terms associated with the effect of the current [7],

$$\frac{\partial \vec{m}}{\partial t} = \gamma \mu_0 \vec{H}_{\text{eff}} \times \vec{m} + \alpha \vec{m} \times \frac{\partial \vec{m}}{\partial t} - (\vec{u} \cdot \vec{\nabla}) \vec{m}$$
$$+ \beta [\vec{m} \times (\vec{u} \cdot \vec{\nabla}) \vec{m}]. \qquad (1)$$

Here the first term describes the precession of the magnetization around the effective field, $\vec{H}_{\text{eff}}$, and the second term is the phenomenological Gilbert damping term describing the relaxation of the system. The following two terms are those associated with a spin-polarized current of density j and polarization P written in terms of the so-called spin-drift velocity, $u = j P g \mu_B / 2 e M_S$ [8]. The permittivity of free space is μ_0, μ_B is the Bohr magneton, γ is the gyromagnetic ratio, g is the electron's spin g factor, e is the electron charge, and M_S is the saturation magnetization. The first of the current-dependent terms describes the adiabatic spin-transfer torque and the second the nonadiabatic torque whose strength is quantified by the β parameter. However, while the damping parameter α is relatively well understood and can be calculated, for instance, via a linear response formulism [9], the contributions to β and the relation to α are still under debate [7,10–12]. The size of β has a transformative influence on the dynamics of a system; e.g., in the case of current-induced DW motion, in the adiabatic limit the maximum domain-wall velocity is the spin-drift velocity when the changing spin-angular momentum of the conduction electrons is fully transferred to DW displacement. Furthermore, for $\beta = 0$, models predict a threshold current for the onset of steady DW motion, while for finite β, this intrinsic threshold depinning current vanishes and, moreover, the subsequent DW velocity is $v_{\text{DW}} = \frac{\beta}{\alpha} u$ up to the critical velocity for the Walker breakdown, given by [10]

$$v_{\text{WB}} = v_c \frac{\alpha}{|\beta - \alpha|}. \qquad (2)$$

*klaeui@uni-mainz.de

TABLE I. Comparison of reported values of β, α and their ratio for permalloy-based systems. TW: transverse DW; VW: vortex DW; DVW: double vortex DW; VC: vortex core; SW: spin wave; TR: time resolved; MOKE: magneto-optic Kerr-effect magnetometry; TEM: transmission electron microscopy; DP: depinning; MTXM: magnetic transmission x-ray microscopy; WB: Walker breakdown; PEEM: photoemission electron microscopy; res.: at resonance; STXM: scanning transmission x-ray microscopy. * denotes the current work. † indicates that this technique is only sensitive to the spin-relaxation component of β [14].

System\technique	$\alpha \times 10^2$	$\beta \times 10^2$	β/α	Ref.
SW\TR †	0.82	2	2–3	[14]
SW\TR-MOKE †	0.75 ± 0.03	3.5 ± 1.1	4.7 ± 1.5	[15]
Nanobridge\MOKE	~ 0.8	~ 4	~ 5	[16]
TW hopping\TEM	~ 0.8	1.0 ± 0.4	~ 1.3	[17]
TW\res. DP		40.7 ± 1.8		[18]
TW\I_{DP}	0.77 ± 0.06	4.0 ± 0.5	5.2 ± 0.8	[19]
VW hopping\TEM	~ 0.8	7.3 ± 2.6	~ 9.2	[17]
VW\v_{DW}		0.7		[20]
VW\I_{WB}	0.8	13 ± 1	16	[21]
VW\v_{DW}	0.8 ± 0.2	~ 2.6	~ 3.2	[22]
VW-VC\res.	0.9	1.8	2	[23]
VW-VC res.\STXM	0.6 ± 0.1	6.1 ± 0.6	10.4 ± 0.3	[24]
DVW-VC\MTXM			0.96 ± 0.02	[25]
VC res\TEM	1.6 ± 0.1	15 ± 2	9.2 ± 0.8	[26]
VC\PEEM	0.8	15 ± 7	19	[5]
VC\SEMPA	0.85 ± 0.06	11.9 ± 2.2	14 ± 3	[27]
VC\SEMPA	0.61 ± 0.01	6.7 ± 1.4	11.0 ± 2.5	[*]
TW Py$_{1\%V}$\I_{DP}	0.71 ± 0.03	4.00 ± 0.25	5.6 ± 0.4	[19]
TW Py$_{2.5\%V}$\I_{DP}	0.73 ± 0.04	4.60 ± 0.25	6.3 ± 0.3	[19]
TW Py$_{10\%V}$\I_{DP}	0.76 ± 0.06	6.80 ± 0.25	9.0 ± 0.7	[19]
VW Py$_{1\%Ho}$\I_{WB}	2	30 ± 10	15	[21]
VW Py$_{4\%Ho}$\I_{WB}	8.7	110 ± 15	13	[21]
VW Py$_{10\%Ho}$\I_{WB}	26	160 ± 60	6 ± 2	[21]
VC Py$_{1.73\%Dy}$\SEMPA	3.98 ± 0.12	29 ± 15	7 ± 4	[*]

Here, $v_c = \gamma \mu_0 H_k \Delta/2$ is the critical velocity for DW motion for $\beta = 0$, with Δ the DW width and H_K the magnetostatic field. The field, $H_K = 2K/(\mu_0 M_S)$, is derived from the effective transverse anisotropy K. Hence it can be seen that both DW velocities and the critical velocities depend not only on β, but also on the ratio and relation between β and α. Experimentally, there has been a very wide range of values reported for β between 0.01 and 4.07 [5,13–27], even within the single materials system permalloy, as can be seen in Table I. This has led to suggestions that there are multiple contributions to β. Different proposed theoretical models suggest both an intrinsic contribution due to spin relaxation (β_{sr}) and a truly nonadiabatic contribution (β_{na}) due to the inability of the electrons to track rapid magnetization changes, leading to mistracking for large magnetization gradients [11,12,28]. This is supported by the experimentally observed larger values of β for vortex domain walls compared with transverse domain walls and the large values of β seen for vortex states [5,17,24,26]. However, corresponding measurements of β for narrow DWs in materials with perpendicular magnetic anisotropy, where large magnetization gradients are present, revealed values of β that are not very large [29]. This was

recently explained as being due to an additional topological contribution to β in the case of the vortex-core systems [24].

Theoretical predictions suggest that both spin structure (nonadiabatic mistracking) and material properties (spin relaxation) influence the nonadiabaticity. Experimentally, however, only the effect of the spin structure has been identified [17] with explanations for enhanced values as found in [5,24,26,27]. To probe the effect of the material, one needs in particular a robust technique that allows one to measure the nonadiabaticity for different materials. Different techniques have been used to determine β which often suffer from problems such as pinning of domain walls during domain-wall motion. The most developed technique that has shown robust values for β is vortex-core displacement [5,26,27,30]. In this scheme, the influence of edge roughness on the dynamics is strongly suppressed compared with wires and β can be extracted independently from assumptions of the damping or polarization. To examine the influence of materials properties and therefore identify a possible spin-relaxation mechanism is thus an open challenge, requiring measurements of β for a set spin structure but different materials parameters using a single robust technique.

In this study, we investigate the relationship between β and α by imaging the current-induced displacement of the vortex core in magnetic disks in the vortex state via high-resolution scanning electron microscopy with polarization analysis. Comparing the displacement for different initial chiralities and polarities yields a value of β which is corrected for the Oersted field. We investigate the influence of rare-earth doping using Dy that significantly modifies the damping parameter of the films, while leaving the spin structure largely unaffected. We find that in addition to an expected high value for β associated with the particular spin configuration of the vortex core, an additional large enhancement is seen with Dy doping. Together with an increase in the damping constant α with Dy doping, we deduce a similar scaling of both parameters, shedding light onto the origin of the nonadiabaticity in doped systems.

The samples consist of 4.3-μm-diameter, $\sim$25–27-nm-thick contacted magnetic disks as depicted in the scanning electron microscopy (SEM) image in Fig. 2(c) and are patterned via a standard two-step electron-beam lithography procedure with lift-off processing on naturally oxidized silicon substrates. In the first stage, the disks are patterned, with the magnetic material deposited via electron-beam evaporation in an ultrahigh vacuum (UHV) chamber with a base pressure of 5×10^{-10} mbar. The thickness is determined by way of a calibrated quartz microbalance with deposition rates between 4 and 14 nm per hour for Py and < 2 nm per hour for Dy. A thin ~ 5 nm Au capping layer is used to prevent oxidation. In the case of the dysprosium-doped samples, codeposition is employed. For this, a low-dysprosium rate is set and once a stable rate is achieved, the Py deposition rate is increased to provide the desired nominal doping level. Periodically during growth, the dysprosium deposition rate is checked to ensure uniform doping through the samples. The exact doping concentrations in the final samples were determined via Rutherford backscattering spectroscopy (RBS) and in-house energy-dispersive x-ray (EDX) spectroscopy using continuous unpatterned films grown concurrently with the patterned

layers. In a second lithography step, Cu(80 nm)/Au(10 nm) contacts are patterned at higher deposition rates to allow for electrical contact to the disks. Overall, we analyze more than 10 samples comprising different growth batches, which we combine into two doping level categories: (i) undoped Py and (ii) low-Dy-doped Py (1.73 ± 0.2 at.% from RBS).

In order to characterize the damping of the materials systems, we perform ferromagnetic resonance (FMR) measurements of films grown in the same batch as the disk samples using a vector network analyzer. The samples are placed on a strip line and the $\widetilde{S}_{12}$ transmission parameter was recorded as a function of the in-plane field, H, for different excitation frequencies f_{FMR}. A more detailed description of the FMR measurement and analysis procedure can be found in previous work [31].

For the magnetic imaging, we employ SEM with polarization analysis (SEMPA), a laboratory-based technique with better than 30 nm spatial resolution. Our Omicron system is equipped with electrical contacts for electrical excitation of the sample and a liquid-helium cryostat, permitting measurements at sample temperatures below 30 K [32]. Before imaging, the gold capping layer is removed via 1 kV Ar$^+$ ion sputter cleaning, which is necessary due to the surface sensitivity of the technique [32].

Different initial magnetic configurations of the vortex state were prepared in the disks by saturating the samples with an in-plane magnetic field of ~ 300 mT followed by a rotation of the sample by $\pm 90°$ to set a preferential out-of-plane orientation of the magnetization, before reducing the field to zero. Since a variety of metastable domain configurations can exist for disks of the given geometry [4], a demagnetization procedure was also employed to promote the flux-closure vortex state, resulting in one of the two energetically degenerate vortex chiralities, which were determined by direct imaging. Here, the vortex chirality c refers to a curling of the magnetization clockwise around the vortex core with $c = +1$ or a counterclockwise curling with $c = -1$. The out-of-plane orientation of the magnetization of the vortex core is denoted as the polarity p, with p being either $+1$ or -1 (up or down). The successful realization of the expected polarity was confirmed from the subsequently determined direction of vortex-core displacement with respect to the electron flow direction during current excitations (see Ref. [5] for details). For each initial magnetic state, the disk is imaged at various constant current densities in the sequence $j = 0$, $j = \pm j_i$, $j = \mp 2 j_i$, …, $j = 0$ (see Fig. 2 for current direction definition) for a chosen interval of current density j_i. In order to reduce the thermal load on the samples during current application, imaging was performed at stage temperatures of ~ 30 K. Furthermore, to reduce the effects of thermal drifts of the images, short acquisition times are used, with multiple images combined to provide sufficient signal-to-noise ratio.

The position of the vortex core is extracted using a noise-resistant cross-correlation algorithm which allows for sub-pixel precision in the case of an idealized data set. However, typical resolution for the employed acquisition times is around 20 nm. The magnetic image is first mapped onto the coordinates of the disk by using the topographic secondary electron images. The position of the vortex core is then extracted for the different applied current densities by comparing the states

with an analytical vortex and, in this manner, the current-induced displacement is determined in each case. The procedure automatically corrects for Oersted field-induced disk distortions, which has been shown to be necessary to obtain the correct value of the nonadiabaticity, β [33].

In order to investigate the influence of materials properties on the nonadiabaticity, we start with the well-studied Py system and employ rare-earth doping using Dy to significantly modify the damping of the material, as described above. We first start by characterizing the properties of the different materials. The damping α of the undoped Py and doped Py thin films is determined using ferromagnetic resonance measurements which are presented in Fig. 1. Figure 1(a) presents the absorption spectra at an excitation frequency f_{FMR} of 4.5 GHz for undoped Py (red) and two Dy-doped Py films (black, blue) with an average Dy content of 1.73%. The corresponding full width at half maximum (FWHM) linewidths are 2.0 ± 0.1 mT (red), 12.4 ± 1.5 mT (blue), and 13.2 ± 1.5 mT (black). The increase in linewidth is consistent with an increased damping of the films [34], while the blue and black films show consistent behavior between the different growth batches of the doped films. The field dependence of the resonant frequency for the undoped film is presented in Fig. 1(b). The red line is a fit to the Kittel equation, yielding $M_S = 878.4 \pm 0.3$ kA/m assuming in-plane easy-plane magnetic-shape anisotropy [31]. From the associated evolution in linewidth with frequency, as shown in Fig. 1(c), the damping parameter can be extracted from the slope $(4\pi \alpha \gamma^{-1})$ [31] and, with $\gamma = 176$ MHz/mT, we find a typical low damping of $\alpha = (6.1 \pm 0.1) \times 10^{-3}$. For the doped films, we calculate α from the measured linewidth at 4.5 GHz, assuming no inhomogeneous broadening, which is a reasonable assumption based on the small intercept for the undoped case of 0.4 ± 0.1 mT and literature reports of negligible inhomogeneous broadening for Dy-doped Py in the doping range studied here [34]. The resulting value is $\alpha_{1.73\%\text{Dy}} = (3.98 \pm 0.12) \times 10^{-2}$, in line with the previous results [34]. In addition to the increase in damping with doping, the measurement yields a decrease of M_S by 13% for one 1.73% Dy-doped Py film, which is in good agreement with a $17.5 \pm 7.5\%$ reduction in M_S determined on the same sample using a superconducting quantum interference device (SQUID) magnetometer. The reduction in the effective M_S is due to the antiferromagnetic coupling of the dopant and the host alloy [35,36], and for the films used, M_S remained relatively constant ($<10\%$ variation) in the measured temperature range. We note that we also investigated 8% Dy-doped samples. However, while we do observe very broad resonance spectra for these films, indicating a strongly increased damping in these highly doped samples, a large decrease in the saturation magnetization leads to other metastable magnetic states and so reliable imaging of vortex-core displacement is not possible. The measured and derived values of α and M_S are summarized in Table II.

In order to determine the nonadiabaticity, we use the approach proposed by Heyne *et al.* and Krüger *et al.*, where the β parameter can be extracted from the amplitude and direction of imaged vortex-core displacement for different vortex-state polarities and chiralities under current-induced excitation, as described in Refs. [5,30]. The films are first
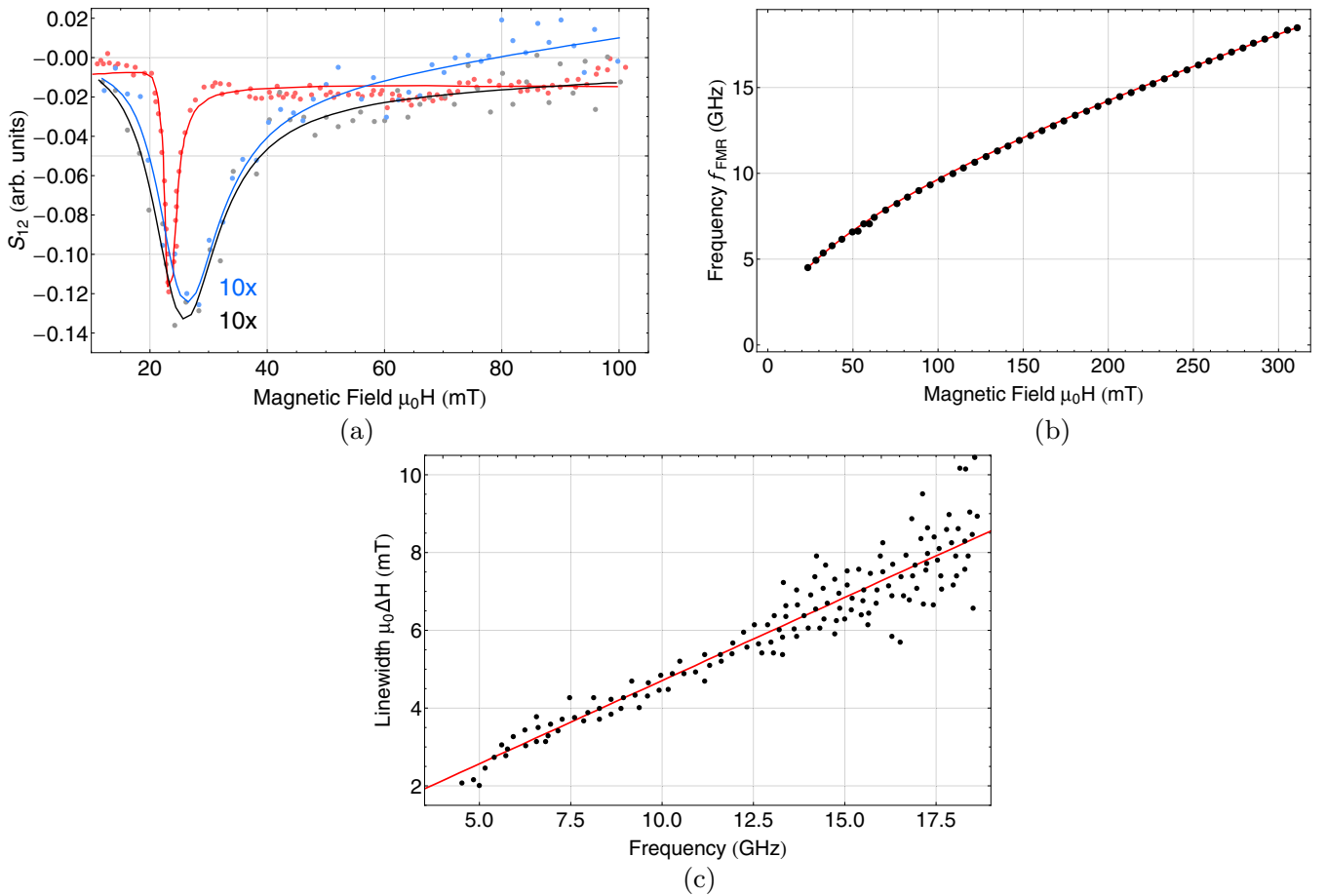
FIG. 1. (a) Ferromagnetic resonance absorption spectra at an excitation frequency f_{FMR} of 4.5 GHz for undoped Py (red) and two doped Py films (1.73%; blue and black). The corresponding FWHM linewidths are 0.20 ± 0.01 Oe (red), 1.24 ± 0.15 Oe (blue), and 1.32 ± 0.15 Oe (black). The thin films were grown alongside the films used for structured samples. For the undoped films, the associated magnetic field dependence of the resonance frequency and the frequency evolution of the linewidth is shown in (b) and (c), respectively.

patterned into disks with a diameter of 4.3 μm and then imaged using scanning electron microscopy with polarization analysis (SEMPA). An SEM image of a typical sample can be seen in Fig. 2 along with typical SEMPA images of the vortex-core displacement. Figures 2(a) and 2(b) show the imaged displacement for the same disk and state for a current density of $\pm 0.5 \times 10^{12}$ Am^{-2}, respectively. As can be seen, the displacement is in opposite directions, as expected from the spin-transfer torque. Furthermore, the displacement direction is seen to be at an angle with respect to the current flow, revealing an influence of the nonadiabaticity in the sample. Since for large displacements the confining potential

TABLE II. Determined parameters of the undoped and low-doped systems.

	Py$_{0\%Dy}$	Py$_{1.73\%Dy}$
M_S (kA/m)	878 ± 0.3	713 ± 33
$\alpha \times 10^2$	0.61 ± 0.01	3.98 ± 0.12
$\beta \times 10^2$	6.7 ± 1.5	29 ± 15
β/α	11.0 ± 2.5	7 ± 4

is expected to display some anharmonicity [37,38], we restrict our analysis to lower current densities for which the displacement vs current density is found to be linear. Such linear behavior is exemplified in Fig. 3(a), where it can again be seen that the displacement direction depends on the magnetic state. According to theory, the adiabatic and nonadiabatic STT lead to vortex-core displacement along the y and x axes, respectively, which reverses on reversing the current direction. In the case of the adiabatic contribution, this is independent of the chirality of the state but reverses on reversing the polarity, whereas the nonadiabatic contribution is independent of both c and p. This is evident by comparing the two blue states, with opposite polarity and the same chirality, displaying opposite displacement in the y direction due to the adiabatic contribution. In addition to the two spin-transfer-torque contributions, there is also the possibility of a parasitic influence of the Oersted field on the vortex-core displacement. The Oersted field can arise due to inhomogeneous current flow and the current flowing vertically from the pads to the structure, and is oriented along the y axis with the direction depending on current flow direction [5]. For a given field direction, this in turn leads to vortex-core displacement along the $\pm x$ axis, depending on the chirality of the state but independent of
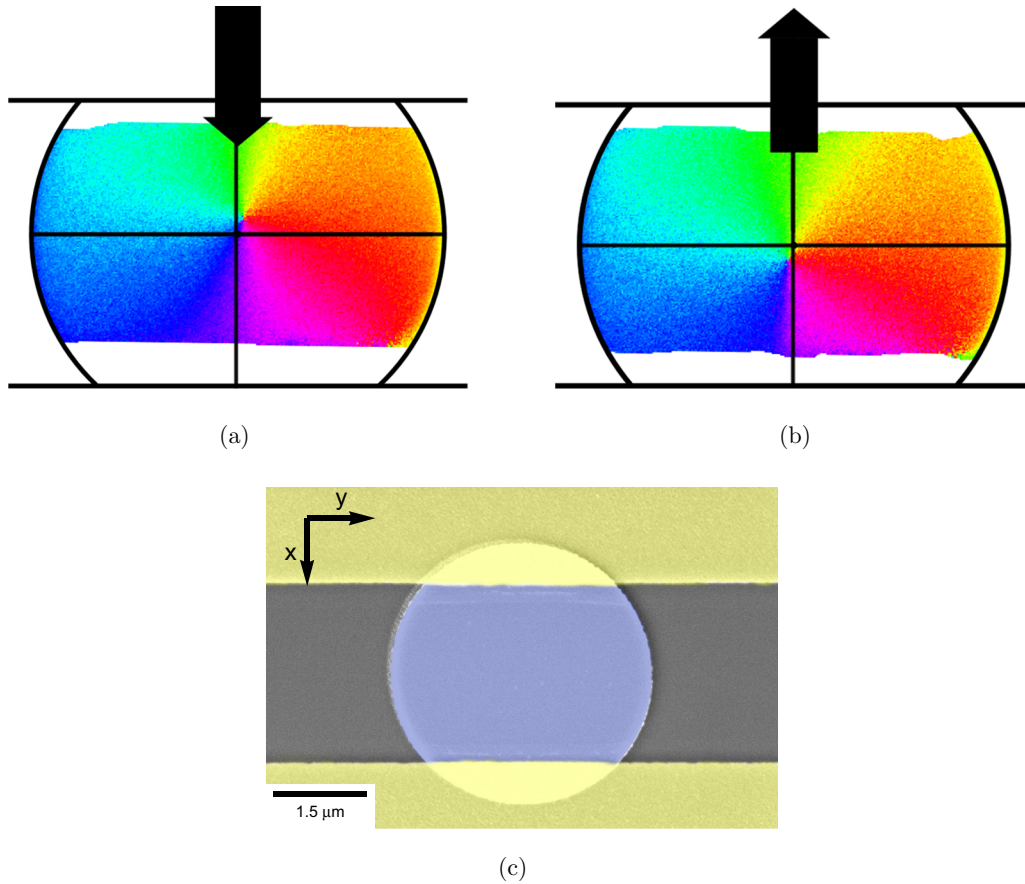
FIG. 2. SEMPA images of the vortex-core displacement for magnetic vortex states of undoped disks with $p = +1$ and $c = +1$. (a),(b) The same disk with $j = +/- 0.5 \times 10^{12}$ Am^{-2}. The black crosses mark the geometrical center of the disk where the vortex is located at zero current. (c) False-color scanning-electron-microscope image of a typical sample. The contact pads are shaded in yellow and the Py disk is shaded in blue. The substrate (gray) is naturally oxidized silicon. Here, the right-handed x-y coordinate system is defined by the visible edges of the contacted disk structure with the x axis being perpendicular to the edges of the contact pads and the y axis being parallel to them. Thus, in this coordinate system, the electric current through the central region of the disk flows parallel to the x axis.

the polarity. This is seen from the difference in the slope of the trajectories of the red and blue states with opposite chirality and polarity, revealing a small contribution from the Oersted field for our samples. From this different dependence of the three contributions on j, p, and c, the coefficient ξ can be extracted using a modified Thiele equation approach as follows [5,27,30]:

$$\xi = \frac{p}{2} \frac{\|G_0\|}{\|D_0\|} \frac{r_{\|(c,p,j)} - r_{\|(-c,-p,j)}}{r_{\perp(c,p,j)}}. \tag{3}$$

The coefficient ξ is in turn related to the nonadiabaticity parameter by $\beta = \frac{\xi}{1+\xi^2}$. For the considered system with a constant M_S, the Thiele equation treats the vortex with its core region as a rigid spin structure that displays emergent quasiparticlelike dynamics that is governed by its topology [30,39]. The resulting equation of motion is based on the gyrocoupling vector G and the dissipation tensor D, which describe the emergent gyrotropic and dissipative forces acting on the spin structure. Both quantities are defined by integrals over the sample volume, which depend on the specific spin configuration and, in particular, on its topology [30,39]. In

Eq. (3), G_0 is the magnitude of this gyrovector and D_0 is the diagonal element of the energy-dissipation tensor with $D_0 = D_{xx} = D_{yy}$ and $D_{zz} = 0$. While both quantities, G_0 and D_0, depend on the magnetic state, the only nonzero contribution to G_0 in the case of the magnetic vortex state is the vortex-core region. Furthermore, $r_\|$ denotes the change of the vortex-core position along the x axis and $r_\perp$ along the y axis. Therefore, the change in position parallel and perpendicular to the current flow corresponds to $r_\|$ and $r_\perp$, respectively. For higher accuracy, we use the slopes of the displacement curves of each sample for the calculation of the nonadiabaticities of each sample, helping to average out the remaining small influence of shallow pinning sites following the exclusion of more strongly pinned states from the analysis [5]. The ratio $\frac{\|D_0\|}{\|G_0\|}$ is determined for our geometry from micromagnetic simulations using standard values for Py [40] by applying a homogeneous current density of 3×10^{11} Am^{-2} to displace the vortex-core region of the two vortex states [$(c; p; j)$ and $(-c; -p; -j)$] within the simulated disk structure for a given ξ value. This yields a value of 3.24 ± 0.01, in good agreement with analytical expressions [5,30]. The micromagnetic simulations were performed using the MICROMAGNUM code
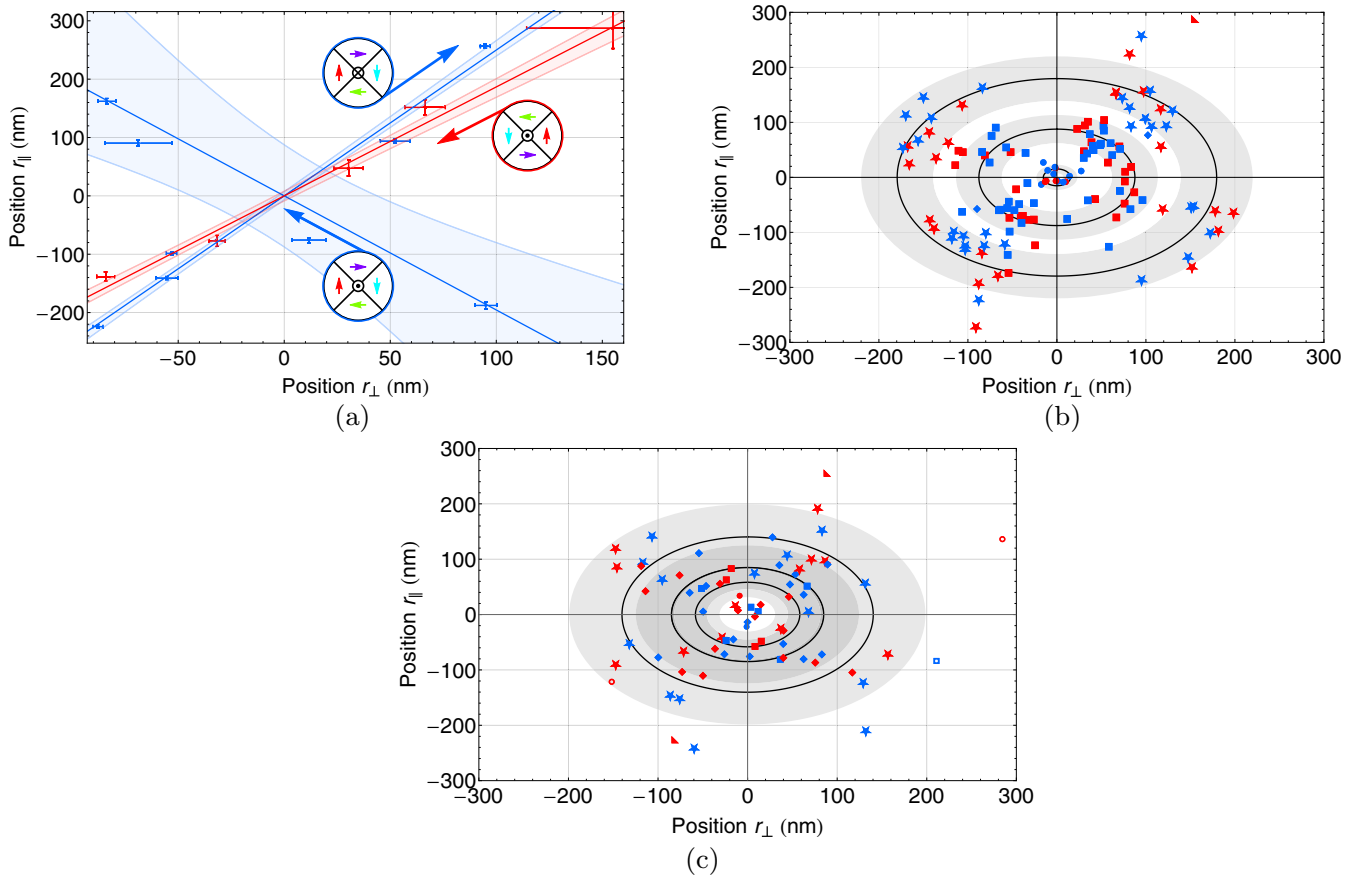
FIG. 3. (a) The extracted displacements for three different states of one disk, as indicated schematically, for varying current densities, plotted along the current direction $r_\parallel$ (x) and also perpendicular, $r_\perp$ (y). The error bars reflect the uncertainty in the determined vortex-core position as determined via a cross-correlation algorithm. Linear regressions were performed for the three states which show a significant difference in the slope, as shown by the highlighted 1σ environment. (b) Collected vortex-core positions for 27-nm-thick undoped Py disks. Magnetic states affected by pinning have been excluded from the plots using the approach pioneered in Ref. [5]. Red/blue corresponds to chirality $c = +/-1$, respectively. The superimposed black circles indicate the mean magnitude of displacement derived from the magnetic states under the influence of current densities of 0.0×10^{11} Am^{-2} (closed circles), 2.7×10^{11} Am^{-2} (closed squares), and 5.4×10^{11} Am^{-2} (stars). For some samples, additional displacements were observed for 4.5×10^{11} Am^{-2} (diamonds) and 8.1×10^{11} Am^{-2} (triangles) with the shaded regions being the associated 1σ areas. (c) The corresponding current-induced vortex-core displacement for the 26-nm-thick doped Py disks. Here, the solid circles indicate the mean magnitude of displacement for current densities of 0.9×10^{11} Am^{-2}, 1.8×10^{11} Am^{-2}, and 2.7×10^{11} Am^{-2} derived from the corresponding states indicated by closed rectangles, diamonds, and stars, respectively. For some samples, additional states have been measured at current densities of 0.0×10^{11} Am^{-2} (open circles) and 5.4×10^{11} Am^{-2} (open squares). The observed displacement of the vortex cores follows the predicted behavior [30] and thus the polarities p can be inferred from the slope of the trajectories.

[40]. The disk structures were simulated on a two-dimensional (2D) grid with 1433×1433 rectangular cuboidal cells having in-plane edge length of 3 nm. The thickness of the structures is simulated using a single 2D layer with a height of 25 nm, which is a good approximation for our samples where no significant variation of the spin structure across the sample thickness is expected.

The collected displacement positions for different current densities and different initial states and samples can be seen in Figs. 3(b) and 3(c) for the undoped and 1.73% Dy-doped samples, respectively. The data points clearly fall into four distinct regions corresponding to a particular angular deflection for each quadrant of the graph and, while the collected data of the two chiralities show discernible regions of overlap, since the influence of the Oersted field is small, the data for the individual samples exhibit significant differences in the slope, as expected by the above outlined theory, showing consistent

behavior between the different states (chirality/polarity combinations). For the doped samples, there is more scatter in the data and there was a greater observed influence of pinning so that fewer data points could be used for robust extraction of the displacement.

Ultimately, the values of β were determined for each individual sample and the weighted average was determined for each doping level, as detailed in Table II. For the undoped Py film, we find $\beta = (6.7 \pm 1.5) \times 10^{-2}$ and a corresponding ratio of β/α of 11.0 ± 2.5. These values are larger than the values from measurements based on spin waves or transverse domain walls for which values of $\beta \approx \alpha$ have been reported, as can be seen in Table I. However, they compare well with similar measurements of β associated with vortex cores, for which enhanced nonadiabaticity has been reported [5,24,26,27]. These results were explained based on an enhanced nonadiabatic contribution for large magnetization

gradients such as present in the vortex-core region [41]; however, to account for the low reported values of β for narrow domain walls in perpendicular magnetic anisotropy materials, a recent combined theoretical and experimental work explained the enhanced β for vortex cores as arising from the topological nature of the spin state, which is consistent with the present work [24].

We now turn our attention to the value of β for the doped sample. Here we find a greatly enhanced value of $\beta = (29 \pm 15) \times 10^{-2}$. We note that the error bar on this value is relatively large due to the spread of the measured values. Analytical models show that the size of the vortex-core spin structure changes only very little as a result of the 17% reduction of M_S [42] due to the rare-earth dopant and this is thus not sufficient to explain the size of the observed effect [24]. Such a dependence of β on doping for the same spin structure shows that there is a clear influence of the materials parameters of the system. It was recently reported that disorder is expected to enhance the nonadiabaticity, even in the absence of spin-flip scattering, due to Elliott-Yafet-type spin relaxation [12], but also additional spin relaxation is expected to increase β [7]. In our case, we have magnetic impurities and hence we expect spin-flip scattering to be important. This therefore implies a similar origin of the enhanced values in each case. Since the damping in such doped films has been explained via the slow-relaxing impurity model, we conclude a connection between this avenue of angular momentum dissipation and the spin relaxation at the heart of nonadiabaticity in the case of the studied rare-earth dopants. This result has a clear implication for the utilization of the spin-torque effect in future devices and highlights the importance of rare-earth doping as a new avenue for tailoring magnetic properties to achieve desirable device characteristics.

[1] Y. Chen, X. Wang, H. Li, H. Xi, Y. Yan, and W. Zhu, IEEE Trans. Very Large Scale Integrat. (VLSI) Sys. **18**, 1724 (2010).

[2] S. S. P. Parkin, M. Hayashi, and L. Thomas, Science **320**, 190 (2008).

[3] S.-K. Kim, K.-S. Lee, Y.-S. Yu, and Y.-S. Choi, Appl. Phys. Lett. **92**, 022509 (2008).

[4] C. A. F. Vaz, M. Kläui, L. J. Heyderman, C. David, F. Nolting, and J. A. C. Bland, Phys. Rev. B **72**, 224426 (2005).

[5] L. Heyne, J. Rhensius, D. Ilgaz, A. Bisig, U. Rüdiger, M. Kläui, L. Joly, F. Nolting, L. J. Heyderman, J. U. Thiele, and F. Kronast, Phys. Rev. Lett. **105**, 187203 (2010).

[6] G. Hrkac, P. S. Keatley, M. T. Bryan, and K. Butler, J. Phys. D: Appl. Phys. **48**, 453001 (2015).

[7] S. Zhang and Z. Li, Phys. Rev. Lett. **93**, 127204 (2004).

[8] M. D. Stiles, W. M. Saslow, M. J. Donahue, and A. Zangwill, Phys. Rev. B **75**, 214423 (2007).

[9] H. Ebert, S. Mankovsky, D. Ködderitzsch, and P. J. Kelly, Phys. Rev. Lett. **107**, 066603 (2011).

[10] A. Thiaville, Y. Nakatani, J. Miltat, and Y. Suzuki, Europhys. Lett. **69**, 990 (2005).

[11] J. Xiao, A. Zangwill, and M. D. Stiles, Phys. Rev. B **73**, 054428 (2006).

[12] C. A. Akosa, W.-S. Kim, A. Bisig, M. Kläui, K.-J. Lee, and A. Manchon, Phys. Rev. B **91**, 094411 (2015).

[13] G. S. D. Beach, M. Tsoi, and J. L. Erskine, J. Magn. Magn. Mater. **320**, 1272 (2008).

[14] K. Sekiguchi, K. Yamada, S.-M. Seo, K.-J. Lee, D. Chiba, K. Kobayashi, and T. Ono, Phys. Rev. Lett. **108**, 017203 (2012).

[15] J.-Y. Chauleau, H. G. Bauer, H. S. Körner, J. Stigloher, M. Härtinger, G. Woltersdorf, and C. H. Back, Phys. Rev. B **89**, 020403 (2014).

[16] M. C. Hickey, D.-T. Ngo, S. Lepadatu, D. Atkinson, D. McGrouther, S. McVitie, and C. H. Marrows, Appl. Phys. Lett. **97**, 202505 (2010).

[17] M. Eltschka, M. Wötzel, J. Rhensius, S. Krzyk, U. Nowak, M. Kläui, T. Kasama, R. E. Dunin-Borkowski, L. J. Heyderman, H. J. van Driel, and R. A. Duine, Phys. Rev. Lett. **105**, 056601 (2010).

[18] E. Martinez, L. Lopez-Diaz, O. Alejos, and L. Torres, Phys. Rev. B **77**, 144417 (2008).

[19] S. Lepadatu, J. S. Claydon, C. J. Kinane, T. R. Charlton, S. Langridge, A. Potenza, S. S. Dhesi, P. S. Keatley, R. J. Hicken, B. J. Hickey, and C. H. Marrows, Phys. Rev. B **81**, 020413 (2010).

[20] G. S. D. Beach, C. Knutson, C. Nistor, M. Tsoi, and J. L. Erskine, Phys. Rev. Lett. **97**, 057203 (2006).

[21] T. A. Moore, M. Kläui, L. Heyne, P. Möhrke, D. Backes, J. Rhensius, U. Rüdiger, L. J. Heyderman, J.-U. Thiele, G. Woltersdorf, C. H. Back, A. Fraile Rodríguez, F. Nolting, T. O. Mentes, M. A. Niño, A. Locatelli, A. Potenza, H. Marchetto, S. Cavill, and S. S. Dhesi, Phys. Rev. B **80**, 132403 (2009).

[22] L. Thomas, R. Moriya, C. Rettner, and S. S. Parkin, Science **330**, 1810 (2010).

[23] R. Moriya, L. Thomas, M. Hayashi, Y. B. Bazaliy, C. Rettner, and S. S. P. Parkin, Nat. Phys. **4**, 368 (2008).

[24] A. Bisig, C. A. Akosa, J.-H. Moon, J. Rhensius, C. Moutafis, A. von Bieren, J. Heidler, G. Kiliani, M. Kammerer, M. Curcic, M. Weigand, T. Tyliszczak, B. Van Waeyenberge, H. Stoll, G. Schütz, K.-J. Lee, A. Manchon, and M. Kläui, Phys. Rev. Lett. **117**, 277203 (2016).

[25] G. Meier, M. Bolte, R. Eiselt, B. Krüger, D.-H. Kim, and P. Fischer, Phys. Rev. Lett. **98**, 187202 (2007).

[26] S. D. Pollard, L. Huang, K. S. Buchanan, D. A. Arena, and Y. Zhu, Nat. Commun. **3**, 1028 (2012).

[27] S. Rößler, S. Hankemeier, B. Krüger, F. Balhorn, R. Frömter, and H. P. Oepen, Phys. Rev. B **89**, 174426 (2014).

[28] S. Bohlens and D. Pfannkuche, Phys. Rev. Lett. **105**, 177201 (2010).

[29] C. Burrowes, A. P. Mihai, D. Ravelosona, J.-V. Kim, C. Chappert, L. Vila, A. Marty, Y. Samson, F. Garcia-Sanchez, L. D. Buda-Prejbeanu, I. Tudosa, E. E. Fullerton, and J.-P. Attane, Nat. Phys. **6**, 17 (2010).

[30] B. Krüger, M. Najafi, S. Bohlens, R. Frömter, D. P. F. Möller, and D. Pfannkuche, Phys. Rev. Lett. **104**, 077201 (2010).

[31] A. Conca, S. Keller, L. Mihalceanu, T. Kehagias, G. P. Dimitrakopulos, B. Hillebrands, and E. T. Papaioannou, Phys. Rev. B **93**, 134405 (2016).

[32] R. M. Reeve, C. Mix, M. König, M. Foerster, G. Jakob, and M. Kläui, Appl. Phys. Lett. **102**, 122407 (2013).

[33] L. Heyne, Ph.D. thesis, Universität Konstanz, 2010.

[34] G. Woltersdorf, M. Kiessling, G. Meyer, J.-U. Thiele, and C. H. Back, Phys. Rev. Lett. **102**, 257602 (2009).

[35] L. T. Baczewski, D. Givord, J. M. Alameda, B. Dieny, J. P. Nozieres, J. P. Rebouillat, and J. J. Prejean, Acta. Phys. Pol. A **83**, 629 (1993).

[36] E. Burzo, Rom. Repts. Phys. **63**, 1316 (2011).

[37] O. V. Sukhostavets, B. Pigeau, S. Sangiao, G. de Loubens, V. V. Naletov, O. Klein, K. Mitsuzuka, S. Andrieu, F. Montaigne, and K. Y. Guslienko, Phys. Rev. Lett. **111**, 247601 (2013).

[38] D. Bedau, M. Kläui, M. T. Hua, S. Krzyk, U. Rüdiger, G. Faini, and L. Vila, Phys. Rev. Lett. **101**, 256602 (2008).

[39] A. A. Thiele, Phys. Rev. Lett. **30**, 230 (1973).

[40] Micromagnum, http://micromagnum.informatik.uni-hamburg.de (unpublished).

[41] G. Tatara and P. Entel, Phys. Rev. B **78**, 064429 (2008).

[42] A. Wachowiak, J. Wiebe, M. Bode, O. Pietzsch, M. Morgenstern, and R. Wiesendanger, Science **298**, 577 (2002).